



# Hollow petal-like $\text{Co}_3\text{O}_4$ nanoflakes as bifunctional electrocatalysts through template-free protocol and structural controlled kinetics in gas evolution

Jun Yang, Liangqin Wei, Tingting Zhao, Tiantian Yang, Jiqian Wang, Wenting Wu, Xiujie Yang, Zhongtao Li\*, Mingbo Wu\*\*

State Key Laboratory of Heavy Oil Processing, School of Chemical Engineering, China University of Petroleum, Qingdao, 266580, China

## ARTICLE INFO

### Article history:

Received 10 March 2019  
Received in revised form  
19 May 2019  
Accepted 17 June 2019  
Available online 18 June 2019

### Keywords:

Bifunctional electrocatalyst  
Self-assemble  
Hollow structure  
 $\text{Co}_3\text{O}_4$   
Overall water splitting

## ABSTRACT

The morphology and porosity of electrocatalysts play essential roles on gas evolution reactions, such as OER and HER in water splitting. Therefore, rational design of highly efficient multifunction electrocatalysts with optimized nanostructures is of great importance for sustainable energy conversion processes. Herein, hollow petal-like  $\text{Co}_3\text{O}_4$  nanoflakes could be readily available through calcining the corresponding MOFs (Metal–organic frameworks) nanoflower precursor, which could be controllable synthesized by a novel template-free protocol. Through modulating reaction conditions, the morphology and porosity of the catalysts could be controlled, which could directly influence on the catalytic activities of OER and HER. The super-hydrophilic hollow petal-like  $\text{Co}_3\text{O}_4$  nanoflakes effectively facilitate mass transfer and ease gas bubbling, which contribute to a promoted bifunctional electrocatalytic activity for both HER and OER, as well as overall water splitting (A stable  $10 \text{ mA cm}^{-1}$  water-splitting current can be reached by just applying 1.67 V, which is comparable to other recently reported catalysts in alkaline media). The hollow  $\text{Co}_3\text{O}_4$  microflowers that reported here confirm the significance of structural features effect on electrocatalyst performance, which will open up a new approach to design high-performance electrode materials for gas evolution reactions.

© 2019 Elsevier Ltd. All rights reserved.

## 1. Introduction

The electrochemical water splitting is a promising strategy to produce clean hydrogen fuel from aqueous solutions [1–3]. However, the sluggish cathodic hydrogen evolution reaction (HER), anodic oxygen evolution reaction (OER) and high energy consumption greatly hinder the development of water electrolysis [4–6]. Currently, noble-metal Pt is the benchmark HER catalysts, while the oxide of Ir or Ru serves as the state-of-the-art priority OER catalysts [7]. However, the exorbitant price and scarcity of these noble-metals restrain their large-scale applications [8–10]. Therefore, it is crucial to explore earth-abundant and catalytically active non-noble-metal catalysts, such as some transition metal oxides [10], chalcogenides [11] and phosphides [12], which have been demonstrated as noticeable electrocatalysts toward the HER and OER reactions in water splitting.

Among these low-cost catalysts, Co-based OER catalysts have emerged as a promising candidate of water splitting catalysts owing to their environmental friendliness, abundant reserves, low cost and thermal stability in alkaline electrolytes [13,14]. As an important kind of spinel oxide,  $\text{Co}_3\text{O}_4$  has received considerable interest as an OER catalyst because of its attractive catalytic activity [15–17]. Recently, a lot of work has been endeavored to design and synthesize advanced nanoscale  $\text{Co}_3\text{O}_4$  catalysts through the following aspects: Firstly, increasing electronic conductivity [18], which can be improved through the introduction of oxygen vacancies [19], heteroatoms doping [20] and coupling with other conductive materials [21]; Secondly, exposing more active sites, which can be achieved by regulating the morphology [22], increasing surface area [23] and modulating crystalline phase through the control of temperature and reaction kinetics [24–26]; More importantly, optimization of surface activity is also playing an essential role in gas evolution reactions (HER and OER). The morphology regulation and size control can change the surface tension to make it more hydrophilic, which prompt the disengagement of gas bubbles and facilitate mass transfer during

\* Corresponding author.

\*\* Corresponding author.

E-mail addresses: [liztao@upc.edu.cn](mailto:liztao@upc.edu.cn) (Z. Li), [wumb@upc.edu.cn](mailto:wumb@upc.edu.cn) (M. Wu).

reaction [27–29]. Despite intensive efforts having been made to develop  $\text{Co}_3\text{O}_4$  toward electrocatalysts, only few of them thoroughly synthesizing morphology-controlled  $\text{Co}_3\text{O}_4$  and understanding the mechanism of formation process. It is necessary to synthesize a kind of  $\text{Co}_3\text{O}_4$  with controllable morphology, clear mechanism of formation and excellent electrocatalytic performance.

Hollow and porous three-dimensional (3D) nanostructured materials have attracted increasing attention due to their remarkable advantages on convenient permeation of electrolytes, shortened transport distance of electrons and enhanced surface active sites [30]. Some reports prove that two-dimensional (2D) nanostructures can effectively expose more catalytically active sites and improve conductivity, like nanosheets and nanoplates [31]. Therefore, developing 3D hollow nanohybrids that are composed of nanosheets will contribute to improving catalytic property in electrochemical reactions. Generally, template-based protocol is one of the most popular methods on synthesis hollow nanostructures [32]. But the template removal process in the template-based methods bring more complications and time-consuming. Recently, some hollow  $\text{Co}_3\text{O}_4$  nanohybrids have been reported through self-template protocol, which avoid tedious template removing process. Li's group reported a novel "self-template" synthetic route to hollow  $\text{Co}_3\text{O}_4$  microspheres, which were composed of porous, ultrathin, single-crystal-like nanosheets [33]. Zhang's team demonstrated the self-template strategy could effectively synthesize hierarchical  $\text{Co}_3\text{O}_4$  porous nanotubes via the oxidation-induced transformation of Co-Asp (cobalt–aspartic acid) and Kirkendall effect [34]. However, it still faces great challenge on synthesis hollow nanostructures with size and morphology control, optimized micro/mesoporosity by high reproducibility and facile synthesis procedure [35–37]. As far as MOFs (Metal–organic frameworks) are concerned, it is one of the versatile precursors for preparing unique metal compounds/carbon hybrids, which have the unique structures and morphology-controlled as well as better conductivity through thermal pyrolysis. Therefore, it is highly significant yet challenging to utilize the MOFs precursors to controllable synthesis of  $\text{Co}_3\text{O}_4$  with unique morphology, high conductivity and understanding the mechanism of the structure effect on gas evolution reaction.

Herein, a well-defined hollow petal-like Co-MOFs nanoflakes was synthesized through a facile and novel template-free protocol, whose structure could be controlled through modulating reaction condition. Generally, adjusting the temperature and kinetics is an ideal method to achieve controllable material morphology and size. The growth mechanism of hollow petal-like Co-MOF nanoflakes was investigated. After calcination, the Co-MOFs precursor was converted to petal-like  $\text{Co}_3\text{O}_4$  nanoflakes, which could be used as bifunctional electrocatalysts in cathode and anode for overall water splitting. The hollow  $\text{Co}_3\text{O}_4$  microflowers exhibit excellent catalytic activity and stability towards overall water splitting owing to the optimized morphology and porosity to facilitate bubbling and mass transfer. (A stable  $10 \text{ mA cm}^{-2}$  water-splitting current can be reached by just applying  $1.67 \text{ V}$  bias, which is comparable to other recently reported catalysts in alkaline media, Table S1). The robust strategy and mechanism investigation will offer new avenue in developing practical applicable electrode materials for overall water splitting.

## 2. Experimental section

### 2.1. Synthesis of Co-MOFs

0.3 g of 2-Aminoterephthalic acid was dissolved into 60 mL of ethanol and heated in an oil bath as the solution A. 0.2 g of

Cobalt(II) acetate tetrahydrate and 0.2 g polyvinyl pyrrolidone (PVP) were dispersed into 40 mL of ethanol as the solution B. Then, solution B was slowly injected into solution A and subsequently heated under refluxing conditions for 20 min. Obtained precipitates were collected by centrifugation, washed with ethanol for three times and dried in an oven at  $60^\circ\text{C}$  for 12 h. Reflux temperature were  $65^\circ\text{C}$ ,  $85^\circ\text{C}$  and  $105^\circ\text{C}$ , respectively, and obtained products were denoted as Co-MOF-65, Co-MOF-85, Co-MOF-105.

### 2.2. Synthesis of c-Co-MOFs

Co-MOF-65, Co-MOF-85, Co-MOF-105 precursors were carbonized under air atmosphere at  $350^\circ\text{C}$  for 2 h, respectively, with a heating rate of  $2^\circ\text{C}\cdot\text{min}^{-1}$ , flower-like  $\text{Co}_3\text{O}_4$  (namely c-Co-MOF-65), hollow flower-like  $\text{Co}_3\text{O}_4$  (namely c-Co-MOF-85) and  $\text{Co}_3\text{O}_4$  sheets (namely c-Co-MOF-105) were obtained after cooled down to room temperature naturally, respectively.

### 2.3. Synthesis of $\text{Co}_3\text{O}_4$ spheres (i.e. c-Co-85)

For comparison, the  $\text{Co}_3\text{O}_4$  spheres sample (namely Co-85) was prepared under the same conditions for synthesizing hollow flower-like  $\text{Co}_3\text{O}_4$  without addition of PVP (namely c-Co-85).

### 2.4. Materials characterization

X-ray powder diffraction (XRD) patterns were collected on an X-ray diffractometer with Cu  $K\alpha$  radiation. Transmission electron microscopy and STEM-HAADF elemental mapping (TEM, JEM-2010UHR, Japan). The Brunauer–Emmett–Teller (BET) specific surface area and pore size distribution were investigated by nitrogen adsorption–desorption isotherms on a sorption analyzer (Micromeritics, ASAP 2050, America). The Raman spectra were performed on a Renishaw DXR Raman spectroscopy system. The elemental valences of the samples were analyzed using X-ray photoelectron spectroscopy (XPS, Thermo Scientific ESCALab250Xi). Contact angle instrument (Solon Tech (Shang Hai) Co., Ltd. SL200B). is used to detect the contact angle of the catalyst.

### 2.5. Electrochemical measurements

Electrochemical measurements were conducted using 760E Bipotentiostat (CH Instruments) as a typical three-electrode system, in which large surface area carbon rod as the counter electrode, Hg/HgO as the reference electrode, and the calcined Co-MOFs were used as the working electrode. Typically, 1 mg catalysts mixed with  $10 \mu\text{L}$  5 wt % Nafion solution was dispersed in  $390 \mu\text{L}$  of ethanol solution and sonicated for 30 min to form a homogeneous ink. The catalyst ink was dropped onto a pre-treated Ni foam (A piece of Ni foam ( $1 \times 1 \text{ cm}^2$ ) was washed with HCl, acetone, and ethanol three times to ensure the removal of oxidation layer), and then dried at  $60^\circ\text{C}$  for 12 h in a vacuum oven (loading:  $1 \text{ mg cm}^{-2}$ ). The HER and OER performances were recorded from the LSV polarization curves in 1 M KOH with a scan rate of  $5 \text{ mV s}^{-1}$ . According to the Nernst equation:  $E(\text{RHE}) = E(\text{Hg}/\text{HgO}) + 0.0592 \text{ pH} + 0.098$ , all the voltage values were converted into the reversible hydrogen electrode (RHE). The corresponding polarization curves shown in this article were calibrated after iR correction. The overall water-splitting system was received using c-Co-MOF-85/NF as both anode and cathode in two-electrode configuration.

### 3. Results and discussion

#### 3.1. Material synthesis and morphological analysis

The synthetic strategy for the  $\text{Co}_3\text{O}_4$  hollow nanoflowers was schematically described in Fig. 1a. Firstly, Cobalt(II) acetate tetrahydrate was dissolved into ethanol with certain amount poly(vinylpyrrolidone) (PVP). Then, organic ligand 2-Aminoterephthalic acid was added into the mixture and reacted at certain temperature (namely Co-MOF-65 at 65 °C, Co-MOF-85 at 85 °C and Co-MOF-105 at 105 °C), which could convert to Co-MOFs through coordination bonds with  $\text{Co}^{2+}$ . In special, the Co-MOFs could be self-assembled into various nanostructures, which could be controlled by modulating heating-up temperature, reaction time and surfactants during wet chemistry process. Subsequently, the Co-MOFs precursor was pyrolyzed at 350 °C under air atmosphere to prepare  $\text{Co}_3\text{O}_4$ /carbon nanohybrids (the calcined Co-MOF-65 named c-Co-MOF-65, the calcined Co-MOF-85 named c-Co-MOF-85 and the calcined Co-MOF-105 named c-Co-MOF-105), and then dispersed in ethanol and drop coated on nickel foam as electrode for overall water splitting.

To investigate the influence of reaction temperature on the structure of Co-MOFs, the Scanning electron microscopy (SEM) images of Co-MOF-65, Co-MOF-85 and Co-MOF-105 are shown in Fig. 1b–d. After reacting 20 min at 65 °C (Fig. 1b), large amount of nanoclusters are self-assembled on substrate with an average diameter of 1  $\mu\text{m}$  in the Co-MOF-65, which are composed by aggregated nanosheets with the thickness around 10 nm. When the reaction temperature rises up to 85 °C, the aggregated nanosheets are found in Co-MOF-85, which become more uniform and larger. These nanosheets eventually self-aligned perpendicular and emanate from the center, which look like the petals of flowers and the diameters are increased to about 2  $\mu\text{m}$ . Meanwhile, from the top view of the sphere in Fig. 1c, the “nanoflowers” are consisted of hollow concave inside, and the hollow nanoflowers of uniform size are evenly distributed and universal (Fig. S1a). In the TEM image of the Co-MOFs-85, the hollow structure of “nanoflowers” is further verified (Fig. S1b). When the solvothermal temperature rise up to 105 °C (Fig. 1d), the “nanoflowers” in the Co-MOF-85 disappear and are replaced by cross-linked nanosheets. Increasing reaction temperature also can accelerate Co cations migration, irregular staked

nanosheets can be identified even after reacted a shorter time (Fig. 1d). At the lower temperature, the growth of nanoflowers are slow down as that in Co-MOF-65 (Fig. 1b). Moreover, PVP seems also play an essential role on modulating the morphologies of the Co-MOFs precursor. Some irregular nanoparticles of Co-MOFs are formed when reacted at 85 °C without introduction of PVP (namely Co-85, and calcined Co-85 is named c-Co-85), which size distribute from 1  $\mu\text{m}$  to 3  $\mu\text{m}$  and the surface roughness become much higher (Fig. S2).

As another parameter, the reaction time also greatly influenced the nanostructure of products. The SEM image of products that reacted at 85 °C after various times were shown in Fig. 2. As shown in Fig. 2a, a large number of small Co-MOFs particles are formed after addition of ligands, which can be consider as the “seeds” for the next stage of growth [38]. When the reaction time prolong to 10 min, a great amount of petal-like nanoflakes with the average size at 300–500 nm are fabricated, which emanative grow from the “nanoseeds” cores (Fig. 2b). After reacted 20 min, the average size of microflowers increase to 1–3  $\mu\text{m}$  with a hollow structure as that of Co-MOF-85 (Fig. 2c). When reacted over 60 min, the morphology change from hollow microflower into irregular staked nanosheets, which are consistent with Co-MOF-105.

Based on the experimental results, the mechanism of Co-MOFs nanoflowers fabrication is put forward in Fig. 2e, which starts from the formation of the crystalline nucleus (Fig. 2a) [39,40]. The PVP plays an important role in the following process to grow the uniform hollow microflowers, which can absorb on the surface of Co-MOFs crystal core along z-axis through strong coordination interaction between pyrrolidone and Co cation. PVP directs the growth direction of Co-MOFs, which is similar to the mechanism of action of pour-point depressants [41]. The hydrophobic vinyl groups in PVP back bone orient in outside, which low polarity hinder Co cation from penetrating into core section [42]. Therefore, the crystalline growth along z-axis is slow down, while the nanocrystal continues to extend along x-axis and y-axis to form well-ordered 2D nanosheets. Due to the nanosheets emanate growth from the crystalline nucleus, a petal-like nanoflakes like in Fig. 2b is formed. As the reaction time is prolonged, more ligands and Co cations in the solution are continuously deposited onto the Co-MOFs nanoflowers, which size become much larger (Fig. 2c).

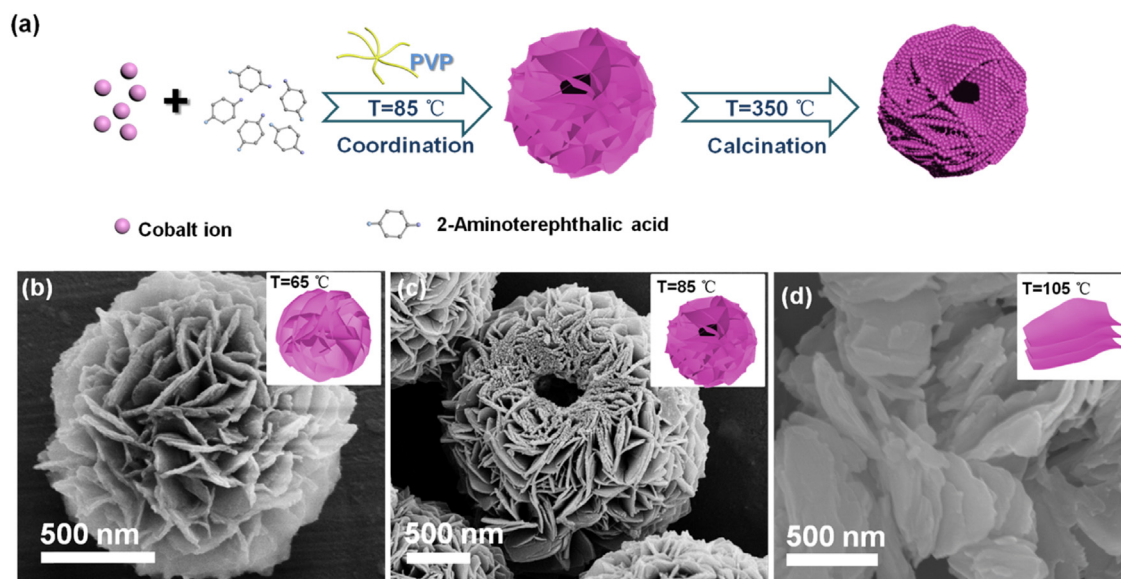


**Fig. 1.** (a) Schematic illustration of the preparation of  $\text{Co}_3\text{O}_4$ ; the SEM images of (b–d) Co-MOF-65, Co-MOF-85 and Co-MOF-105, respectively. The inset of (b–d) is the schematic representation of Co-MOFs at different temperatures.

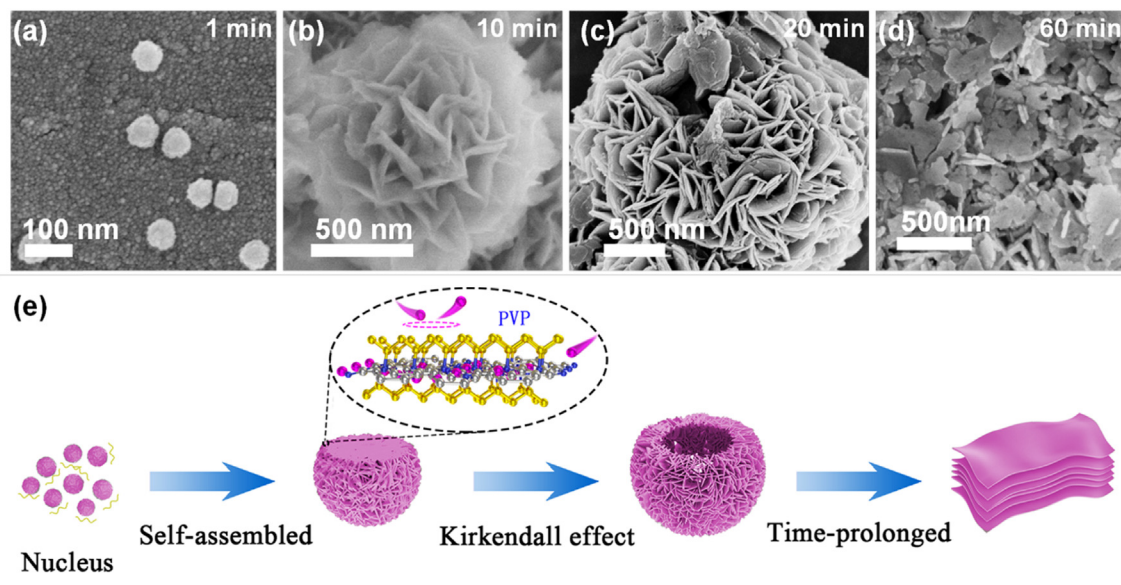


Fig. 2. The SEM images (a–d) of the precursor products obtained at different stages; (e) The schematic illustration of the evolution of precursor products at different stages.

Meanwhile some Co cations in the core section also gradually migrate outward to react with the ligands, which driven by the concentration differential [34]. With the consumption of cobalt ions, the Co-MOFs in the core sections are gradually dissolved to form a hollow structure. When Co cations in the core section are gradually depleted through the reaction with the ligands in solution, the concaves inside nanoflowers become too larger to keep the connection between nanoflakes. So the nanoflowers are broken into irregular staked nanosheets as shown in Fig. 2d.

### 3.2. Material characteristics and analyses

In previously report,  $\text{Co}_3\text{O}_4$  was proved as an effective catalyst in overall water splitting [16,18,26]. It is generally required to perform

post-treatment of the Co-MOFs to achieve enhanced catalytic activity and the target catalysts ( $\text{Co}_3\text{O}_4$ ) with desired morphology and dimension. Since PVP protects the morphology of Co-MOFs during the calcination process, Co-MOFs is successfully converted to  $\text{Co}_3\text{O}_4$ /carbon hybrid nanostructures, which have excellent electrocatalytic performance. Therefore, the serials of  $\text{Co}_3\text{O}_4$  catalysts with various nanostructure were prepared by annealing the Co-MOFs precursors in atmosphere. From the SEM images, the morphology of calcined Co-MOFs are almost the same as its precursors except a slightly shrink of the nanosheets after pyrolysis (Fig. 3a–b and Fig. S3). The calcined Co-MOF-65 (c-Co-MOF-65) still retains the microflowers structure and the diameter is reduced to about 800 nm (Fig. S3a). Meanwhile, the calcined Co-MOF-85 (c-Co-MOF-85) is consisted with uniformly hierarchical hollow

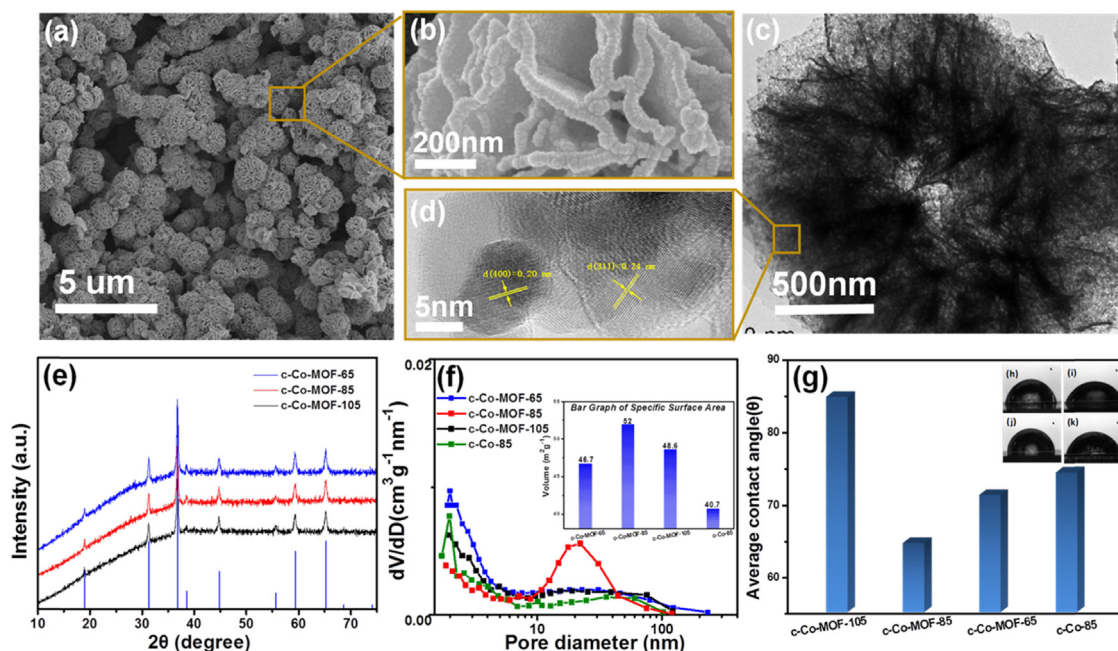


Fig. 3. SEM images of (a–b) c-Co-MOF-85; TEM and HRTEM images (c–d) of c-Co-MOF-85; (e) XRD patterns; (f) pore-size distribution curve. The inset of (f) is bar graph of specific surface area; (g) Contact angle for hydrophilicity test. The inset of contact angle test digital image of (h) c-Co-MOF-105, (i) c-Co-MOF-85, (j) c-Co-MOF-105 and (k) c-Co-85.

microflowers without obvious aggregation and severe cracking (Fig. 3a). The magnified image in Fig. 3b and Fig. S4 show that there are numerous  $\text{Co}_3\text{O}_4$  nanoparticles (with an average diameter of 10 nm) uniformly adhere together in the nanoflakes of hollow microflowers. The high-resolution (HR)TEM image (Fig. 3d) clearly shows lattice fringes inside these particles with interplanar distance of 0.20 nm and 0.24 nm, which correspond to the spacing of the (400) and (311) planes of  $\text{Co}_3\text{O}_4$ .

In order to identify the components in the calcined products, X-ray diffraction (XRD) patterns were recorded and presented in Fig. 3e. The well-defined peaks can all be identified in all samples, which ascribe to  $\text{Co}_3\text{O}_4$  (JCPDS card No. 42–1467). Furthermore, the structures of the calcined samples were also characterized by Raman spectrum (Fig. S5a). The similar peaks appearing at 481, 523, 619 and 689  $\text{cm}^{-1}$  are found in all samples, which correspond to the vibration peaks of  $E_g$ ,  $F_{2g}$ ,  $F_{2g}$  and  $A_{1g}$  of the spinel  $\text{Co}_3\text{O}_4$ . Additionally, the broad peak appearing at 523  $\text{cm}^{-1}$  corresponds to the  $A_{1g}$  vibrational peak of the Co–O bond. To get deeper insight into the detailed surface element make-up of the hollow microflowers, XPS measurements were performed and presented in Figs. S5b and S5c. Very similar data of all samples are obtained: the Co 2p spectrum presents two major peaks with binding energies of 780.1 and 795.5 eV, corresponding to Co 2p<sub>1/2</sub> and Co 2p<sub>3/2</sub>, respectively. The binding energy difference between the peaks of Co 2p<sub>3/2</sub> and Co 2p<sub>1/2</sub> splitting is approximately 15.4 eV, demonstrating the presence of  $\text{Co}^{3+}$  (779.92 and 795.14 eV) and  $\text{Co}^{2+}$  (781.08 and 796.58 eV), which are characteristic peaks for the  $\text{Co}_3\text{O}_4$  phase [43,44]. Furthermore, the ratio analysis of the peaks in XPS spectra was shown in Table S2, which indicated all samples were composed of C, O, N and Co. All the experiment data mentioned above indicate almost the same chemical structure between each sample.

The Brunauer–Emmett–Teller (BET) surface area were investigated by the  $\text{N}_2$  sorption measurements to identify the differences of porosity between various catalysts. Experiment data reveal that c-Co-MOF-85 possesses the largest BET specific surface area of 52  $\text{m}^2 \text{g}^{-1}$  compared with c-Co-MOF-65, c-Co-MOF-105 and c-Co-85 due to the hollow structure (Fig. 3f Inset and Fig. S6). Meanwhile, the pore size distribution curves indicate that c-Co-MOF-85 has a

higher rate of mesoporous (10–45 nm) in Fig. 3f, which have been proved to facilitate the mass transfer previously [22]. To further study the influences of the hollow structure on mass transfer and bubbling generation, hydrophilicity test through contact angle test was carried out. As the control sample, nickel sheet has hydrophobic properties with a contact angle of 103.27° (Fig. S7). Interestingly, after coating of as-prepared samples, the surface of nickel sheet convert to hydrophilic (Fig. 3g). While the c-Co-MOF-85 coating exhibits the smallest contact angle (64.81°) and reflects the best hydrophilicity (The contact angles of c-Co-MOF-65, c-Co-MOF-105 and c-Co-85 are 71.53°, 85.29°, and 74.69°, respectively). In general, the “supra-hydrophilic” (i.e., supra-aerophobic or low bubble adhesive) electrode surface underwater can prompt the disengagement process of gas bubbles and improve compatibility of the catalysts interface with electrolyte and ions [27,45,46]. Therefore, the dead area caused by generated bubbles is reduced with the increasing of hydrophilicity. Therefore, the regular hollow petal-like nanoflakes of c-Co-MOF-85 is able to change catalysts wetting behavior, increase surface area and optimize pore size, which will enhance the performance for gas evolution reaction.

### 3.3. Electrochemical performance

The electrocatalytic OER performances of the as-prepared samples were evaluated by typical three electrode system in Ar-saturated 1 M KOH aqueous electrolyte. The polarization curves after iR correction are displayed in Fig. 4a, all as-perpared samples exhibit improved catalytic activity than bare Ni foam, which demonstrate that the activity of  $\text{Co}_3\text{O}_4$  in OER [47,48]. The c-Co-MOF-65, c-Co-MOF-105 and c-Co-85 display a high onset potential of 1.608 V (vs. RHE), 1.608 V (vs. RHE) and 1.552 V (vs. RHE) at 10  $\text{mA cm}^{-2}$  in OER, respectively. While the anodic current recorded on c-Co-MOF-85 presents lowest sharp onset potential of 1.544 V at 10  $\text{mA cm}^{-2}$  with greatly intensified OER current, which indicate that the unique hollow structure can significantly improve the catalytic activity. Specifically, the Tafel slopes for c-Co-MOF-65, c-Co-MOF-85, c-Co-MOF-105 and c-Co-85 are 108.75, 77.47, 104.5 and 100.74  $\text{mV dec}^{-1}$  respectively (Fig. 4c and Fig. S8a). The lowest Tafel

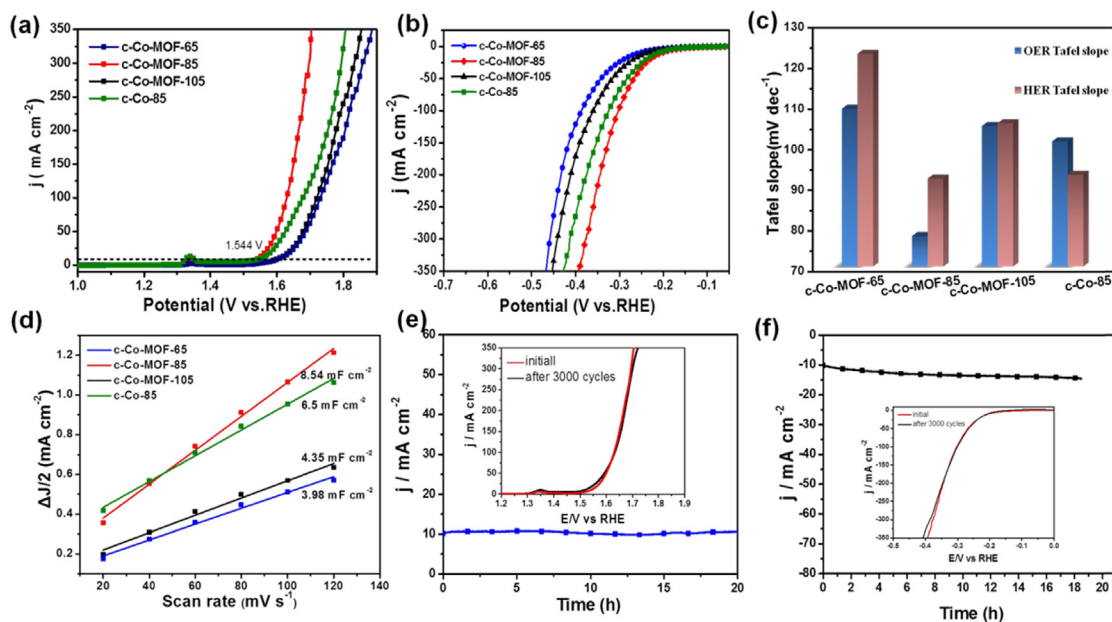


**Fig. 4.** The polarization curves (a and b) and (c) Tafel slopes of OER and HER on c-Co-MOF-65, c-Co-MOF-85, c-Co-MOF-105 and c-Co-85; (d) Plots showing the extraction of the double-layer capacitances ( $C_{dl}$ ); (e) Chronoamperometric curve of c-Co-MOF-85 at 1.544 V (vs. RHE). The inset of (e) is polarization curves of initial and 3000<sup>th</sup> cycles. (f) Chronoamperometric curve of c-Co-MOF-85 at -0.203 V (vs. RHE). The inset of (f) is polarization curves of initial and 3000<sup>th</sup> cycles.

slope of c-Co-MOF-85 represents the accelerated mass transfer during OER performance due to the superior hollow morphology. As shown in Fig. 4e, the durability of c-Co-MOF-85 is examined by chronopotentiometry, and the current density is still maintained at  $10.57 \text{ mA cm}^{-2}$  under the potential of 1.544V after 20 h test. Moreover, the catalyst was further examined by cyclic voltammogram and  $j$ -V curves (Fig. 4e, inset). After 3000 cycles, the anodic current density keeps similar to the fresh catalyst electrode with a negligible decay, which confirms its excellent durability in further.

The electrochemical surface area (ECSA) was further investigated by the cyclic voltammograms (CV) technique, and the ECSA was positive correlated with the double layer capacitance ( $C_{dl}$ ) of catalyst (Fig. S9). In Fig. 4d, the  $C_{dl}$  of c-Co-MOF-85 ( $8.54 \text{ mF cm}^{-2}$ ) is over two times larger than that of c-Co-MOF-65 ( $3.98 \text{ mF cm}^{-2}$ ) and c-Co-MOF-105 ( $4.35 \text{ mF cm}^{-2}$ ), which demonstrate that the high catalytic activity of hollow microflowers can expose more active sites for oxygen generation. Furthermore, impedance spectroscopy measurements was also significant parameters to evaluate the electrode kinetics, and the small charge-transfer resistance indicated a fast charge-transfer rate. Electrochemical impedance spectroscopy measurements of c-Co-MOF-65, c-Co-MOF-85, c-Co-MOF-105 and c-Co-85 were performed at an applied potential of 1.54 V versus RHE from 100 kHz to 0.01 Hz in 1 M KOH. In Fig. S10, the lowest  $R_{ct}$  of c-Co-MOF-85 ( $7.4 \Omega$ ) indicate the lowest charge transfer resistance during OER ( $10.5 \Omega$  and  $11.1 \Omega$  of c-Co-MOF-65 and c-Co-MOF-105, respectively). The results of EIS and  $C_{dl}$  are consistent with BET, polarization curves and Tafel Slope characterizations, which further illustrate that the unique petal-like  $\text{Co}_3\text{O}_4$  nanoflakes can optimize supra-hydrophilic surface and improve charge transfer capability.

The electrocatalytic HER activities of the synthesized materials were assessed in the same electrolyte of OER. As shown in Fig. 4b, c-Co-MOF-85 displays outstanding activities during HER with only 203 mV overpotential at  $10 \text{ mA cm}^{-2}$ . In contrast, c-Co-MOF-65, c-Co-MOF-105 and c-Co-85 held the overpotential of 256 mV, 239 mV and 213 mV at the current density of  $10 \text{ mA cm}^{-2}$ , respectively. The high electrochemical activity of c-Co-MOF-85 attributes to the unique petal-like nanoflakes and supra-hydrophilic surface, which offer more accessible active surface areas for the permeation of electrolyte during HER. The superior HER activity of c-Co-MOF-85 is also confirmed by the smaller Tafel slope of  $91.55 \text{ mV dec}^{-1}$  (Tafel slopes of c-Co-MOF-65, c-Co-MOF-105 and c-Co-85 are  $122.23 \text{ mV dec}^{-1}$ ,  $105.19 \text{ mV dec}^{-1}$  and  $92.47 \text{ mV dec}^{-1}$ , respectively). The durability of c-Co-MOF-85 was evaluated at  $-203 \text{ mV}$  versus RHE (Fig. 4f). After 20 h, the current density of  $10 \text{ mA cm}^{-2}$  is rather stable with imperceptible decay. This result is also confirmed by the almost overlapped 1st and 3000th LSV curves (Fig. 4f, Inset). All data above indicate that the unique petal-like nanoflakes of c-Co-MOF-85 also contributes to the excellent HER catalytic activity.

Encouraged by the outstanding OER and HER performance, a two-electrode overall water splitting cell was fabricated, which adopted c-Co-MOF-85 as active materials both on anode and cathode. Remarkably, the operation water splitting voltage of c-Co-MOF-85 cell at the current density of  $10 \text{ mA cm}^{-2}$  is as low as 1.67 V, which is comparable to other recently reported catalysts in alkaline media (Table S1). Furthermore, the water splitting can be operated at 1.839 V when catalytic current density exceeds  $50 \text{ mA cm}^{-2}$ . More importantly, c-Co-MOF-85 not only has high catalytic activity, but also has great durability. As shown in Fig. 5b, the long-term

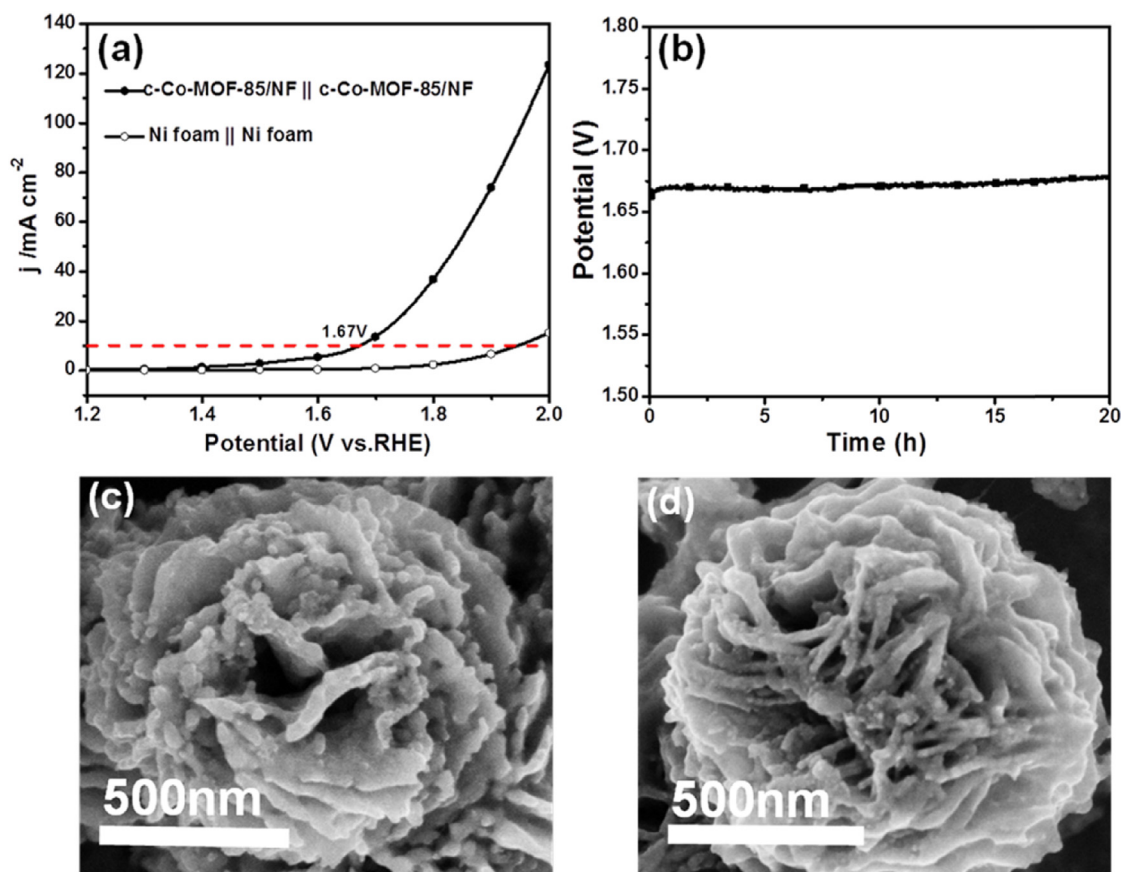


Fig. 5. (a) LSV polarization curves of c-Co-MOF-85 and Ni foam substrate as a bifunctional catalyst in 1 M KOH for water splitting; (b) Long-term stability of the c-Co-MOF-85 bifunctional catalyst at a constant voltage of 1.67 V for 20 h the SEM images of (c) and (d) are the OER and HER after long-term stability of water splitting.

stability of c-Co-MOF-85 for 20 h in 1 M KOH is operated at the constant potential of 1.67 V (Fig. 5b) without detectable current decay. The morphology have not changed greatly after water splitting (Fig. 5c and d), which also demonstrate the promising practical applications for overall water splitting. In general, the catalytic performance of petal-like  $\text{Co}_3\text{O}_4$  nanoflakes in overall water splitting can rival the majority of reported bifunctional electrocatalysts (Table S1). All in all, the high-surface-area of the hollow structure of c-Co-MOF-85 ensure the sufficient exposure and better utilization of electroactive sites, largely contributing to high reaction kinetics at low overpotentials for both HER and OER. Furthermore, the hollow architecture and hierarchical porosity lead to superhydrophilic surface, which provide smooth pathways for the infiltration of electrolytes and rapid emission of bubbles (i.e.,  $\text{O}_2$  and  $\text{H}_2$ ) [49]. The supra-durability of  $\text{Co}_3\text{O}_4$  is kept during long-term operation, and the c-Co-MOF-85 bifunctional catalyst long-term catalyzes for 20 h without detectable decay.

#### 4. Conclusion

In summary, a unique hollow petal-like Co-MOFs nanoflakes was self-assembled through a readily scalable template free protocol. The growth mechanism and structural control methods were thoroughly investigated. After calcination, hollow petal-like  $\text{Co}_3\text{O}_4$  nanoflakes can be readily available from the Co-MOFs nanoflower precursors, and it exhibit super-hydrophilic and large surface area. The supra-hydrophilic surface underwater can prompt the disengagement process of gas bubbles and improve compatibility of the catalyst interface with electrolytes and ions. As the result, the catalytic performance of both the HER and OER are significantly promoted. The catalytic performance of petal-like  $\text{Co}_3\text{O}_4$  nanoflakes in overall water splitting can rival the majority of reported bifunctional electrocatalysts (a stable  $10 \text{ mA cm}^{-1}$  water-splitting current can be reached by applying just 1.67 V), which confirms the significance of structural control effect on electrocatalysts performance in gas evolution reactions. The hierarchical  $\text{Co}_3\text{O}_4$  hollow microflowers structures will be new approach to design other metal oxides as high-performance electrode materials for a broad range of electrochemical applications.

#### Notes

The authors declare no competing financial interest.

#### Acknowledgements

This work was supported by the National Natural Science Foundation of China (Grant Nos. 21572269, 51873231, 21502227), and the Fundamental Research Funds for the Central Universities (17CX05015, 15CX08005 A), the Financial Support from Taishan Scholar Project, the Key Research and Development Program of Shandong Province, China (2017GX40118).

#### Appendix A. Supplementary data

Supplementary data to this article can be found online at <https://doi.org/10.1016/j.electacta.2019.06.105>.

#### References

- [1] Y. Yan, R.W. Crisp, J. Gu, B.D. Chernomordik, G.F. Pach, Ashley R. Marshall, J.A. Turner, M.C. Beard, Multiple exciton generation for photoelectrochemical hydrogen evolution reactions with quantum yields exceeding 100%, *Nat. Energy* 2 (5) (2017) 17052.
- [2] N. Mahmood, Y. Yao, J.W. Zhang, L. Pan, X. Zhang, J.J. Zou, Electrocatalysts for hydrogen evolution in alkaline electrolytes: mechanisms, challenges, and prospective solutions, *Adv. Sci.* 5 (2) (2018) 1700464.
- [3] W. Zhao, T. Xu, T. Li, Y. Wang, H. Liu, J. Feng, S. Ding, Z. Li, M. Wu, Amorphous iron(III)-Borate nanolattices as multifunctional electrodes for self-driven overall water splitting and rechargeable zinc-air battery, *Small* (2018), e1802829.
- [4] H. Fei, J. Dong, Y. Feng, C.S. Allen, C. Wan, B. Voloskiy, M. Li, Z. Zhao, Y. Wang, H. Sun, P. An, W. Chen, Z. Guo, C. Lee, D. Chen, I. Shakir, M. Liu, T. Hu, Y. Li, A.I. Kirkland, X. Duan, Y. Huang, General synthesis and definitive structural identification of  $\text{MN}_4\text{C}_4$  single-atom catalysts with tunable electrocatalytic activities, *Nat. Catal.* 1 (1) (2018) 63–72.
- [5] Q. Zhao, Z. Yan, C. Chen, J. Chen, Spinels: controlled preparation, oxygen reduction/evolution reaction application, and beyond, *Chem. Rev.* 117 (15) (2017) 10121–10211.
- [6] Y. Jiao, Y. Zheng, M. Jaroniec, S.Z. Qiao, Design of electrocatalysts for oxygen- and hydrogen-involving energy conversion reactions, *Chem. Soc. Rev.* 44 (8) (2015) 2060–2086.
- [7] K.Y. Zou, Z.X. Li, Controllable syntheses of MOF-derived materials, *Chemistry* 24 (25) (2018) 6506–6518.
- [8] Y.P. Zhu, C. Guo, Y. Zheng, S.Z. Qiao, Surface and interface engineering of noble-metal-free electrocatalysts for efficient energy conversion processes, *Acc. Chem. Res.* 50 (4) (2017) 915–923.
- [9] S. Ghosh, R.N. Basu, Multifunctional nanostructured electrocatalysts for energy conversion and storage: current status and perspectives, *Nanoscale* 10 (24) (2018) 11241–11280.
- [10] Z. Li, L. Wei, W.J. Jiang, Z. Hu, H. Luo, W. Zhao, T. Xu, W. Wu, M. Wu, J.S. Hu, Chemical state of surrounding iron species affects the activity of Fe-Nx for electrocatalytic oxygen reduction, *Appl. Catal. B* 251 (2019) 240–246.
- [11] M. Shen, C. Ruan, Y. Chen, C. Jiang, K. Ai, L. Lu, Covalent entrapment of cobalt-iron sulfides in N-doped mesoporous carbon: extraordinary bifunctional electrocatalysts for oxygen reduction and evolution reactions, *ACS Appl. Mater. Interfaces* 7 (2) (2015) 1207–1218.
- [12] W. Xi, G. Yan, Z. Lang, Y. Ma, H. Tan, H. Zhu, Y. Wang, Y. Li, Oxygen-Doped nickel iron phosphide nanocube arrays grown on Ni foam for oxygen evolution electrocatalysis, *Small* (2018), 1802204.
- [13] F. Lyu, Q. Wang, S.M. Choi, Y. Yin, Noble-metal-free electrocatalysts for oxygen evolution, *Small* 15 (1) (2019), 1804201.
- [14] J. Kim, O. Gwon, O. Kwon, J. Mahmood, C. Kim, Y. Yang, H. Lee, J.H. Lee, H.Y. Jeong, J.B. Baek, G. Kim, Synergistic coupling derived cobalt oxide with nitrogenated holey two-dimensional matrix as an efficient bifunctional catalyst for metal-air batteries, *ACS Nano* 13 (5) (2019) 5502.
- [15] X. Deng, H. Tüysüz, Cobalt-oxide-based materials as water oxidation catalyst: recent progress and challenges, *ACS Catal.* 4 (10) (2014) 3701–3714.
- [16] M. Yu, Z. Wang, C. Hou, Z. Wang, C. Liang, C. Zhao, Y. Tong, X. Lu, S. Yang, Nitrogen-Doped  $\text{Co}_3\text{O}_4$  mesoporous nanowire arrays as an additive-free air-cathode for flexible solid-state zinc-air batteries, *Adv. Mater.* 29 (15) (2017), 201602868.
- [17] X. Zou, J. Su, R. Silva, A. Goswami, B.R. Sathe, T. Asefa, Efficient oxygen evolution reaction catalyzed by low-density Ni-doped  $\text{Co}_3\text{O}_4$  nanomaterials derived from metal-embedded graphitic  $\text{C}_3\text{N}_4$ , *Chem. Commun.* 49 (68) (2013) 7522–7524.
- [18] T.Y. Ma, S. Dai, M. Jaroniec, S.Z. Qiao, Metal-organic framework derived hybrid  $\text{Co}_3\text{O}_4$ -carbon porous nanowire arrays as reversible oxygen evolution electrodes, *J. Am. Chem. Soc.* 136 (39) (2014) 13925–13931.
- [19] Y. Wang, T. Zhou, K. Jiang, P. Da, Z. Peng, J. Tang, B. Kong, W.-B. Cai, Z. Yang, G. Zheng, Reduced mesoporous  $\text{Co}_3\text{O}_4$  nanowires as efficient water oxidation electrocatalysts and supercapacitor electrodes, *Adv. Energy Mater.* 4 (16) (2014) 1400696.
- [20] W. Xu, Z. Lu, X. Lei, Y. Li, X. Sun, A hierarchical Ni-Co-O@Ni-Co-S nanoarray as an advanced oxygen evolution reaction electrode, *Phys. Chem. Chem. Phys.* 16 (38) (2014) 20402–20405.
- [21] S. Chen, J. Duan, M. Jaroniec, S.Z. Qiao, Three-dimensional N-doped graphene hydrogel/NiCo double hydroxide electrocatalysts for highly efficient oxygen evolution, *Angew. Chem.* 52 (51) (2013) 13567–13570.
- [22] L. Yu, H. Hu, H.B. Wu, X.W. Lou, Complex hollow nanostructures: synthesis and energy-related applications, *Adv. Mater.* 29 (15) (2017).
- [23] Y. Lu, L. Yu, M. Wu, Y. Wang, X.W.D. Lou, Construction of complex  $\text{Co}_3\text{O}_4$ @ $\text{Co}_3\text{V}_2\text{O}_8$  hollow structures from metal-organic frameworks with enhanced lithium storage properties, *Adv. Mater.* 30 (1) (2018).
- [24] J.H. Lee, Y.J. Sa, T.K. Kim, H.R. Moon, S.H. Joo, A transformative route to nanoporous manganese oxides of controlled oxidation states with identical textural properties, *J. Mater. Chem.* 2 (27) (2014) 10435–10443.
- [25] S.K. Mazloomi, N. Sulaiman, Influencing factors of water electrolysis electrical efficiency, *Renew. Sustain. Energy Rev.* 16 (6) (2012) 4257–4263.
- [26] J. Huang, J. Chen, T. Yao, J. He, S. Jiang, Z. Sun, Q. Liu, W. Cheng, F. Hu, Y. Jiang, Z. Pan, S. Wei,  $\text{CoOOH}$  nanosheets with high mass activity for water oxidation, *Angew. Chem.* 54 (30) (2015) 8722–8727.
- [27] C. Tang, H.F. Wang, Q. Zhang, Multiscale principles to boost reactivity in gas-involving energy electrocatalysis, *Acc. Chem. Res.* 51 (4) (2018) 881–889.
- [28] M. Qiao, C. Tang, L.C. Tanase, C.M. Teodorescu, C. Chen, Q. Zhang, M.-M. Titirici, Oxygenophilic ionic liquids promote the oxygen reduction reaction in Pt-free carbon electrocatalysts, *Mater. Horizon.* 4 (5) (2017) 895–899.
- [29] K. Qian, Z.D. Chen, J.J. Chen, Bubble coverage and bubble resistance using cells with horizontal electrode, *J. Appl. Electrochem.* 28 (10) (1998) 1141–1145.
- [30] X. Gao, H. Zhang, Q. Li, X. Yu, Z. Hong, X. Zhang, C. Liang, Z. Lin, Hierarchical

- NiCo<sub>2</sub>O<sub>4</sub> hollow microcuboids as bifunctional electrocatalysts for overall water-splitting, *Angew. Chem. Int. Ed.* 55 (21) (2016) 6290–6294.
- [31] Y. Fan, N. Zhang, L. Zhang, H. Shao, J. Wang, J. Zhang, C. Cao, Synthesis of small-sized freestanding Co<sub>3</sub>O<sub>4</sub> nanosheets with improved activity for H<sub>2</sub>O<sub>2</sub> sensing and oxygen evolution, *J. Electrochem. Soc.* 160 (2) (2013) F218–F223.
- [11] J. Feng, Y. Dong, Y. Yan, W. Zhao, T. Yang, J. Zheng, Z. Li, M. Wu, Extended lattice space of TiO<sub>2</sub> hollow nanocubes for improved sodium storage, *Chem. Eng. J.* 373 (2019) 565–571.
- [33] J. Zhao, Y. Zou, X. Zou, T. Bai, Y. Liu, R. Gao, D. Wang, G.D. Li, Self-template construction of hollow Co<sub>3</sub>O<sub>4</sub> microspheres from porous ultrathin nanosheets and efficient noble metal-free water oxidation catalysts, *Nanoscale* 6 (13) (2014) 7255–7262.
- [34] H. Wang, S. Zhuo, Y. Liang, X. Han, B. Zhang, General self-template synthesis of transition-metal oxide and chalcogenide mesoporous nanotubes with enhanced electrochemical performances, *Angew. Chem.* 55 (31) (2016) 9055–9059.
- [35] J.-H. Lee, Gas sensors using hierarchical and hollow oxide nanostructures: overview, *Sensor. Actuator. B Chem.* 140 (1) (2009) 319–336.
- [36] S. Wu, L. Li, H. Xue, K. Liu, Q. Fan, G. Bai, J. Wang, Size controllable, transparent, and flexible 2D silver meshes using recrystallized ice crystals as templates, *ACS Nano* 11 (10) (2017) 9898–9905.
- [37] H. Rao, S. Ye, F. Gu, Z. Zhao, Z. Liu, Z. Bian, C. Huang, Morphology controlling of all-inorganic perovskite at low temperature for efficient rigid and flexible solar cells, *Adv. Energy Mater.* 8 (23) (2018) 1800758.
- [38] H. He, Q. Gan, H. Wang, G.-L. Xu, X. Zhang, D. Huang, F. Fu, Y. Tang, K. Amine, M. Shao, Structure-dependent performance of TiO<sub>2</sub>/C as anode material for Na-ion batteries, *Nano Energy* 44 (2018) 217–227.
- [39] L. Larini, D. Leporini, A manifestation of the Ostwald step rule: molecular-dynamics simulations and free-energy landscape of the primary nucleation and melting of single-molecule polyethylene in dilute solution, *J. Chem. Phys.* 123 (14) (2005) 485.
- [40] Y. Zhang, C. Wang, H. Hou, G. Zou, X. Ji, Nitrogen doped/carbon tuning yolk-like TiO<sub>2</sub> and its remarkable impact on sodium storage performances, *Adv. Energy Mater.* 7 (4) (2017) 1600173.
- [41] T.V. Fremel, M.A. Zubova, M.É. Yunovich, T.N. Mitsova, Mechanism of action of pour-point depressants, *Chem. Technol. Fuels Oils* 29 (8) (1993) 400–403.
- [42] D. Su, K. Kretschmer, G. Wang, Improved electrochemical performance of Na-ion batteries in ether-based electrolytes: a case study of ZnS nanospheres, *Adv. Energy Mater.* 6 (2) (2016) 1501785.
- [43] F. Wu, X. Zhang, T. Zhao, R. Chen, Y. Ye, M. Xie, L. Li, Hierarchical mesoporous/macroporous Co<sub>3</sub>O<sub>4</sub> ultrathin nanosheets as free-standing catalysts for rechargeable lithium–oxygen batteries, *J. Mater. Chem.* 3 (34) (2015) 17620–17626.
- [44] C. Guan, A. Sumboja, H. Wu, W. Ren, X. Liu, H. Zhang, Z. Liu, C. Cheng, S.J. Pennycook, J. Wang, Hollow Co<sub>3</sub>O<sub>4</sub> nanosphere embedded in carbon arrays for stable and flexible solid-state zinc-air batteries, *Adv. Mater.* 29 (44) (2017), 201704117.
- [45] Z. Lu, W. Zhu, X. Yu, H. Zhang, Y. Li, X. Sun, X. Wang, H. Wang, J. Wang, J. Luo, X. Lei, L. Jiang, Ultrahigh hydrogen evolution performance of under-water "superhydrophobic" MoS<sub>2</sub> nanostructured electrodes, *Adv. Mater.* 26 (17) (2014) 2683–2687, 2615.
- [46] N. Han, K.R. Yang, Z. Lu, Y. Li, W. Xu, T. Gao, Z. Cai, Y. Zhang, V.S. Batista, W. Liu, X. Sun, Nitrogen-doped tungsten carbide nanoarray as an efficient bifunctional electrocatalyst for water splitting in acid, *Nat. Commun.* 9 (1) (2018) 924.
- [47] Z. Xiao, Y. Wang, Y.-C. Huang, Z. Wei, C.-L. Dong, J. Ma, S. Shen, Y. Li, S. Wang, Filling the oxygen vacancies in Co<sub>3</sub>O<sub>4</sub> with phosphorus: an ultra-efficient electrocatalyst for overall water splitting, *Energy Environ. Sci.* 10 (12) (2017) 2563–2569.
- [48] L. Xu, Q. Jiang, Z. Xiao, X. Li, J. Huo, S. Wang, L. Dai, Plasma-engraved Co<sub>3</sub>O<sub>4</sub> nanosheets with oxygen vacancies and high surface area for the oxygen evolution reaction, *Angew. Chem.* 55 (17) (2016) 5277–5281.
- [49] M.S. Burke, M.G. Kast, L. Trotochaud, A.M. Smith, S.W. Boettcher, Cobalt-iron (oxy)hydroxide oxygen evolution electrocatalysts: the role of structure and composition on activity, stability, and mechanism, *J. Am. Chem. Soc.* 137 (10) (2015) 3638–3648.